Check for updates

ADVANCED MATERIALS TECHNOLOGIES
www.advmattechnol.de

High-Performance Black Phosphorus/Graphitic Carbon Nitride Heterostructure-Based Wearable Sensor for Real-time Sweat Glucose Monitoring

Ecem Ezgi Özkahraman, Zafer Eroğlu, Vladimir Efremov, Arooba Maryyam, Taher Abbasiasl, Ritu Das, Hadi Mirzajani, Berna Akgenc Hanedar, Levent Beker, and Onder Metin**

Wearable, non-invasive glucose sensors capable of accurate and continuous monitoring are crucial for managing metabolic conditions, yet achieving high sensitivity and stability in these devices remains challenging. In this work, a black phosphorus/graphitic carbon nitride (BP-gCN) heterostructure is presented, engineered to leverage phosphorus-nitrogen interactions for enhanced nonenzymatic electrochemical glucose oxidation activity. Compared to pristine gCN, the BP-gCN heterostructure demonstrates a significantly improved electrochemical surface area and ≈2 fold reduction in the charge transfer resistance, achieving a remarkable glucose sensitivity of 4.75 µA mM^{-1} cm^{-2} in artificial sweat. Density functional theory (DFT) calculations reveal stronger glucose adsorption and higher charge transfer on the BP-gCN heterostructure than the pristine gCN surface. These theoretical insights complement the experimental findings, highlighting the superior electrocatalytic performance of the heterostructure and the role of the oxidized BP surface. The developed BP-gCN sensor is integrated into a wearable platform with microfluidic layers and a near-field communication chip, forming a battery-free conformal skin patch. In vivo demonstrations confirmed its ability to enable real-time sweat glucose monitoring. This high-performance nonenzymatic wearable glucose sensor highlights the potential of heterostructure designs for seamless health management and next-generation biosensing platforms for personalized, continuous monitoring.

1. Introduction

In recent years, wearable biosensors have emerged as transformative platforms for personalized healthcare, enabling continuous, noninvasive physiological biomarker monitoring and delivering real-time feedback to users outside traditional clinical settings.[1–3] Rapid progress in flexible materials, scalable manufacturing processes, wireless communication protocols, and miniaturized electronics has accelerated the development and deployment of advanced wearable devices.[4–7] Despite this progress, current commercial wearable sensors predominantly monitor basic parameters like heart rate and body temperature and therefore fail to capture insightful molecular-level information crucial for comprehensive health assessment. Recent research has focused on integrating chemical sensors into wearable devices capable of analyzing biological fluids such as interstitial fluid (ISF), tears, saliva, and sweat, providing detailed information on key biomarkers.[8–12] For

E. E. Özkahraman, O. Metin
Department of Materials Science and Engineering
College of Engineering
Koç University
Istanbul 34450, Turkiye
E-mail: ometin@ku.edu.tr

The ORCID identification number(s) for the author(s) of this article can be found under https://doi.org/10.1002/admt.202500106

© 2025 The Author(s). Advanced Materials Technologies published by Wiley-VCH GmbH. This is an open access article under the terms of the Creative Commons Attribution-NonCommercial License, which permits use, distribution and reproduction in any medium, provided the original work is properly cited and is not used for commercial purposes.

DOI: 10.1002/admt.202500106

E. E. Özkahraman, Z. Eroğlu, V. Efremov, O. Metin
Department of Chemistry
College of Sciences
Koç University
Istanbul 34450, Turkiye

A. Maryyam
Department of Electrical and Electronics Engineering
College of Engineering
Koç University
Istanbul 34450, Turkiye

T. Abbasiasl, L. Beker
Department of Biomedical Sciences and Engineering
College of Engineering
Koç University
Istanbul 34450, Turkiye
E-mail: lbeker@ku.edu.tr

instance, diabetes mellitus, a chronic disease characterized by irregular glucose levels in the blood, is typically monitored using glucometers.[13] These devices require users to prick their fingers multiple times a day to measure blood glucose levels, which does not provide for continuous monitoring. In this regard, chemical biosensors integrated into wearable devices, such as skin patches, tattoos, and contact lenses, offer a promising approach for continuous and painless monitoring of glucose levels.[14–16] Among these strategies, sweat-based glucose sensors are particularly promising, as they leverage a naturally secreted, easily accessible fluid, enabling truly noninvasive and continuous glucose monitoring with minimal user discomfort.[17]

To date, a wide range of measurement techniques, including colorimetric, fluorescent, photoelectrochemical, and electrochemical methods have been explored for detecting glucose in sweat.[18–21] Among these methods, electrochemical sensing is particularly attractive for wearable applications due to its rapid response, low power requirements, ease of miniaturization, high sensitivity, selectivity, and straightforward fabrication processes.[22] However, the majority of the reported wearable electrochemical glucose sensors require the use of an enzyme, glucose oxidase (GOx) or glucose dehydrogenase (GDH), which converts the glucose oxidation into an electrical signal.[23,24] While enzymatic sensors offer excellent selectivity, their stability is often compromised by environmental fluctuations in temperature and pH, ultimately reducing their operational lifespan and reliability in real-world, on-body conditions.[25] Moreover, the high cost of enzymes significantly hinders the scalability and long-term affordability of enzymatic sensors, posing a serious economic barrier to widespread adoption in wearable healthcare systems. To address these challenges, there is a growing emphasis on the development of stable, robust, and cost-effective novel materials capable of nonenzymatic glucose oxidation.

Recently, a variety of materials, including metals,[26,27] metal oxides,[28,29] alloys[30,31] and carbon nanocomposites[12,32] have been investigated for nonenzymatic glucose oxidation. While these materials have demonstrated promising performance in glucose detection, they suffer from significant challenges, such as poor selectivity/sensitivity, surface poisoning, and high costs. Additionally, the use of metal-based materials for wearable sensors has several drawbacks, including non-biocompatibility and the need for high pH conditions, as the metal surface requires hydroxide ions for the glucose oxidation reaction.[33] To address these challenges, researchers have focused on developing methods that generate a localized alkaline environment, facilitating the use of metallic materials as a nonenzymatic glucose sensor.[34,35] However, these approaches require high voltage for sensor activation, which poses drawbacks in terms of energy efficiency and necessitates additional pretreatment steps. Consequently, metal-free carbon-based materials have recently gained attention for their superior electron transfer kinetics and resistance to surface poisoning.[36,37] Nevertheless, pure carbon-based materials such as graphene are typically inactive toward the oxidation of alcoholic groups, limiting their effectiveness for electrochemical glucose sensing.[38] Therefore, exploring novel materials such as gCN and its heterostructures with other non-metallic materials is crucial for wearable nonenzymatic glucose sensing, as these materials show promise for advancing the field.

gCN, a polymeric semiconductor composed of C and N atoms, is promising for wearable sensors owing to its 2D structure, large surface area, biocompatibility, and chemical stability.[39,40] gCN is known for its intrinsic peroxidase-like activity,[41] and its applications for electrochemical glucose sensing have been previously investigated.[42–44] Despite the promising potential of gCN for glucose oxidation, significant challenges remain, including high electron-hole recombination rates and low electrocatalytic activity, which we aim to address through innovative heterostructure design with complementary non-metallic materials. On the other hand, BP, a mono-elemental 2D semiconducting material composed of earth-abundant phosphorus atoms, features a tunable bandgap ranging from 0.3 to 2.1 eV, high charge carrier mobility, and excellent biocompatibility, making it particularly suitable for sensor applications.[45] The electrocatalytic activity of BP and its composites has been widely explored, with a focus on the enhanced electrocatalytic performance of oxidized BP (oBP). The superior stability of oBP in glucose dehydrogenation further supports its potential in sensor applications.[46] Additionally, the high surface area of BP nanosheets contributes to increased oxidation current, further enhancing its effectiveness in electrochemical sensing.[47] The oxidation process generates P═O redox sites, enhancing electron transport and improving overall sensor performance, especially when combined with materials such as reduced graphene oxide (rGO).[48] While the oBP sites formed on pristine black phosphorus provide active centers for electrochemical reactions, the inherent instability of pristine BP leads to its further degradation under ambient conditions, resulting in unreliable and irreproducible sensing signals over time.[49] Therefore, forming heterostructures with stable materials is necessary to ensure controlled and limited oxidation of BP. Recent research emphasizes the promise of BP-gCN heterostructures, where P-N coordination significantly enhances the charge transfer while increasing the stability of BP, suggesting them as strong candidates for electrochemical sensing.[50,51] Despite these promising attributes and recent advancements, the full potential of BP-gCN heterostructure for nonenzymatic glucose oxidation in wearable configuration remains unexplored. This gap presents a crucial opportunity to develop a robust, sensitive, and stable electrochemical sensor for glucose detection, which could significantly enhance continuous glucose monitoring capabilities in wearable devices.

R. Das, H. Mirzajani, L. Beker
Department of Mechanical Engineering
College of Engineering
Koç University
Istanbul 34450, Turkiye

B. Akgenc Hanedar
Department of Physics
College of Sciences
Koç University
Istanbul 34450, Turkiye

B. Akgenc Hanedar
Department of Physics
College of Sciences
Kirklareli University
Kirklareli 39100, Turkiye

O. Metin
Koç University Surface Science and Technology Center (KUYTAM)
İstanbul 34450, Türkiye

© 2025 The Author(s). Advanced Materials Technologies published by Wiley-VCH GmbH

2365709x, 2025, 17, Downloaded from https://advanced.onlinelibrary.wiley.com/doi/10.1002/admt.202500106 by Koc University, Wiley Online Library on [05/12/2025]. See the Terms and Conditions (https://onlinelibrary.wiley.com/terms-and-conditions) on Wiley Online Library for rules of use; OA articles are governed by the applicable Creative Commons License

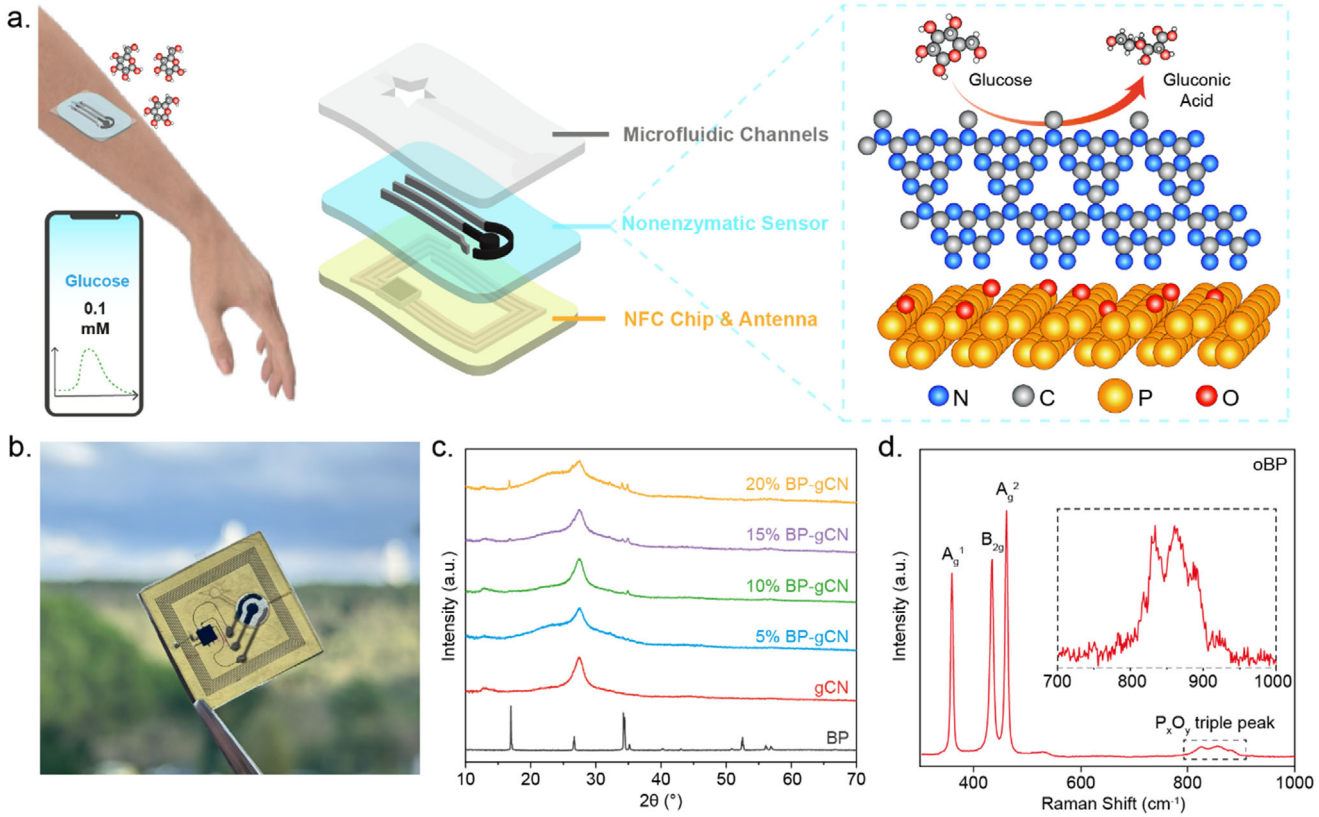


Figure 1. Schematic illustration of the nonenzymatic patch and structural characterizations. a) Designed wearable non-enzymatic sweat patch with layers including microfluidic channels for sweat collection (left), non-enzymatic sensor array, and wireless communication layer by NFC (middle), schematic representation of BP-gCN showing the oxidation of glucose to gluconic acid on the surface (right). b) Photograph of the fabricated device. c) XRD patterns of gCN and 5, 10, 15, 20 wt% BP-gCN. d) Raman spectra of oBP.

In this study, we present a novel approach that integrates rational material design with state-of-the-art sensor technologies to develop a battery-free, flexible, wearable, and nonenzymatic electrochemical glucose sensor. The sensor, based on the BP-gCN heterostructures, operates at physiological pH for sweat glucose detection with a sensitivity of 1.1 μA mM^{-1} cm^{-2} in PBS and 4.75 μA mM^{-1} cm^{-2} in artificial sweat. To optimize the composition for enhanced glucose sensing, BP-gCN heterostructures with varying BP ratios (5, 10, and 20 wt%) were synthesized using a one-step ultrasound assisted liquid phase exfoliation method, and characterized with advanced techniques. The structural characterization of the BP-gCN heterostructures revealed that the constructed P-N interactions in BP-gCN heterostructure improved the glucose oxidation by increasing the electrochemical active surface area (ECSA) and reducing the charge transfer resistance (R_{ct}) almost two-fold, compared to the pristine gCN, prompting us to investigate these superior glucose sensing results through DFT calculations. The glucose adsorption on gCN and BP-gCN was compared, revealing the stronger adsorption and higher charge transfer on the latter surface, which suggests the improved catalytic efficiency for glucose oxidation. Notably, the surface oxides on BP provide additional redox-active sites, which further enhance the glucose oxidation process and contribute to the superior electrochemical performance of the heterostructure. To demonstrate in vivo applicability, the synthesized heterostructures were drop-cast onto screen-printed carbon electrodes (SPCE) and integrated with electronics and microfluidic layers to develop a battery-free wearable skin patch. On-body electrochemical evaluations were conducted wirelessly, with real-time monitoring performed via a smartphone using a commercial near field communication (NFC) chip.

2. Results and Discussion

2.1. Synthesis and Characterization of BP-gCN Heterostructures

To construct a nonenzymatic wearable glucose sensor, we designed a 2D material based heterostructures composed of BP and gCN as the electrochemical sensor layer, integrated between a microfluidic sweat collection platform and a wireless communication module equipped with NFC technology, as illustrated in **Figure** 1a and shown in Figure 1b. First, gCN was synthesized according to the well-established thermal polycondensation method, while BP was fabricated via a mineralizer assisted chemical vapor transport strategy. Subsequently, ultrasound-assisted liquid phase exfoliation was utilized to prepare the targeted BP-gCN heterostructures. The loading ratio of BP into gCN was systematically varied to optimize the heterostructure's performance and evaluate its synergistic impact on electrocatalytic activity.

© 2025 The Author(s). Advanced Materials Technologies published by Wiley-VCH GmbH

2365709x, 2025, 17, Downloaded from https://advanced.onlinelibrary.wiley.com/doi/10.1002/admt.202500106 by Koc University, Wiley Online Library on [05/12/2025]. See the Terms and Conditions (https://onlinelibrary.wiley.com/terms-and-conditions) on Wiley Online Library for rules of use; OA articles are governed by the applicable Creative Commons License

To gain comprehensive insight into the crystallinity and phase composition of the as-prepared materials, powder-XRD analysis was employed. As shown in Figure 1c, two characteristic main peaks of gCN are observed at $2\theta = 27.3°$ (diffraction from the (002) plane) for the stacking of conjugated tri-s-triazine rings and at $2\theta = 13.2°$ (diffraction from the (100) plane) for in-plane interactions.[40] Moreover, the XRD pattern of BP confirms the orthorhombic crystal structure, with the diffraction peaks at $2\theta =$ 16.9, 34.2, and 52.5, corresponding to the (020), (040), and (060) planes, respectively (JCPDS card no. 73–1358).[52] After investigating the crystallinity of pristine materials, XRD patterns of binary heterostructures were collected and compared with them. Figure 1c shows an increasing trend in the BP peak $\approx 2\theta = 34.5°$ (diffraction from the (040) plane) and the peak at $2\theta = 17°$ (diffraction from the (020) plane)[53] as the loading ratio increases. Additionally, a slight shift of the gCN (100) facet peak to lower angles is observed, indicating a decrease in crystallite size and an increase in lattice strain. These results confirm the successful construction of the targeted BP-gCN binary heterostructure.

In the Raman spectrum given in Figure 1d, three characteristic Raman shifts of BP were observed. These Raman shifts correspond to the out-of-plane phonon mode A_g^1 at 360.9 cm^{-1}, and the in-plane phonon modes $B_{2\ g}$ and A_g^2 at 438.6 and 465.5 cm^{-1}, respectively.[46] More importantly, three peaks ≈800–900 cm^{-1} are assigned to the Raman active modes of phosphorus oxides, confirming the oxidized form of BP.[54] The surface oxides on BP contribute significantly to glucose oxidation by creating additional redox-active sites and facilitating an efficient electron transfer between glucose molecules and the catalyst surface, leading to an improved electrochemical response. This increase in electrochemical performance emphasizes the critical role of surface oxides in optimizing glucose sensing applications.

The UV-VIS absorption of the BP-gCN heterostructures was measured, and the bandgaps were determined by using Tauc plots, as shown in Figure S1 (Supporting Information). The analysis reveals that the addition of BP to gCN results in a narrowed bandgap, which indicates improved charge separation. This reduction in bandgap contributes to the observed decrease in R_{ct}, as a narrower bandgap facilitates more efficient electron transfer pathways. Improved charge separation and reduced recombination rates are essential for maintaining a high and stable current response in electrochemical sensing. These characteristics suggest that the oxidized BP-gCN heterostructure can effectively facilitate electron transfer between the sensing surface and the target analyte, thereby enhancing detection sensitivity by enabling faster and more efficient charge transfer.

The morphological and topological features of BP-gCN heterostructures were characterized using SEM, TEM, and AFM analyses. SEM images of gCN revealed a 2D lamellar structure with irregularly curved folds at the edges, while BP exhibited a flake-like morphology with a smooth surface, as shown in Figure S2 (Supporting Information). In the BP-gCN heterostructure, both materials retained their distinct structural features without any topological changes, indicating the formation of a strong interaction between them, as depicted in **Figure 2a**. Consistent with the SEM observations, TEM analysis revealed a layered, mesoporous polymeric structure for gCN, while BP displayed a flat, nanoleaf-like structure (Figure S3, Supporting Information). The TEM image of BP-gCN (Figure 2b) further confirmed the interaction between the two components at the nanoscale, with both morphologies remaining intact. Additionally, further TEM images in Figure S4 (Supporting Information) support this nanoscale integration. According to AFM analysis, the thickness of the as-prepared materials was measured to be 19 nm for gCN and 50 nm for BP, as shown in Figure S5 (Supporting Information). The lateral size of the BP-gCN heterostructure (Figure 2c) decreased to 4 nm at the nanoscale compared to gCN, while it increased compared to BP.

Furthermore, XPS analysis was performed to confirm the oxide formation on the BP surface and the surface chemistry of the BP-gCN heterostructure (Figure 2d–f). The XPS survey spectrum of the BP-gCN heterostructure (Figure S6, Supporting Information) confirms the presence of all expected elements (C, N, P, O) and the absence of any impurities. In the high-resolution XPS spectrum of the C 1s region, the peak at 284.5 eV was attributed to the standard reference carbon, while the peak at 286.2 eV corresponds to carbon atoms bonded to nitrogen (sp^3-hybridized), bridging the heptazine rings in gCN. The dominant peak at 287.9 eV is associated with the C═N bonding in the triazine ring of gCN. A shift of 0.13 eV toward higher binding energies in the C═N peak for BP-gCN suggests an interaction between BP and gCN, likely via electron transfer from gCN to BP.[55] In the high-resolution XPS spectra of the N 1s region, the peak corresponding to the C═N bonds in the s-triazine aromatic rings of the heterostructure was observed at 398.48 eV compared to 398.42 eV for the pristine gCN, indicating a shift of 0.06 eV to higher binding energies. This shift suggests electron redistribution and strong electronic interaction between BP and gCN. Additionally, the N-$(C)_3$ peak was detected at 399.9 eV for BP-gCN and 400.1 eV for gCN, showing a notable 0.2 eV shift to lower binding energies, further confirming the interaction between BP and gCN. Meanwhile, the C-N peak at 401.1 eV appeared without any alteration, indicating that these groups remain largely unaffected in the heterostructure.[56] In the high-resolution XPS spectra of the P 2p region, two distinct peaks appeared at 129.6 and 130.5 eV, corresponding to the P-P bonds of $2p_{3/2}$ and $2p_{1/2}$, respectively. Additionally, in BP-gCN heterostructure, a broad oxidation peak at 134.1 eV is readily assigned to the P—O bond of native surface oxide P_xO_y species, while a peak at 133.1 eV is linked to the P—N interaction.[51] Based on the XPS peak area, P_xO_y species cover ≈8.7% of the BP surface. This low amount of native oxide at the top layer, limited by the gCN's stabilizing effect, is still considered sufficient to provide an adequate number of redox-active sites. Compared to pristine BP, a shift to lower binding energies is observed in the BP-gCN heterostructure, consistent with results observed in the high-resolution XPS spectra of C 1s and N 1s regions. The binding energy shifts observed in the C 1s, N 1s, and P 2p regions, along with the formation of P—N interaction and charge transfer from gCN to BP, indicate that the heterostructure is primarily governed by electronic interactions and physisorption. These shifts reflect electron redistribution and interfacial interactions, involving charge transfer and localized bonding, which contribute to the stability of the heterostructure. Such interactions make the BP-gCN heterostructures highly suitable for applications in electrochemical sensors. Moreover, the observed P-N interactions and formation of oBP enhance the structural integrity, further supporting its potential as an electrochemical sensing platform.[57]

© 2025 The Author(s). Advanced Materials Technologies published by Wiley-VCH GmbH

2365709x, 2025, 17, Downloaded from https://advanced.onlinelibrary.wiley.com/doi/10.1002/admt.202500106 by Koc University, Wiley Online Library on [05/12/2025]. See the Terms and Conditions (https://onlinelibrary.wiley.com/terms-and-conditions) on Wiley Online Library for rules of use; OA articles are governed by the applicable Creative Commons License

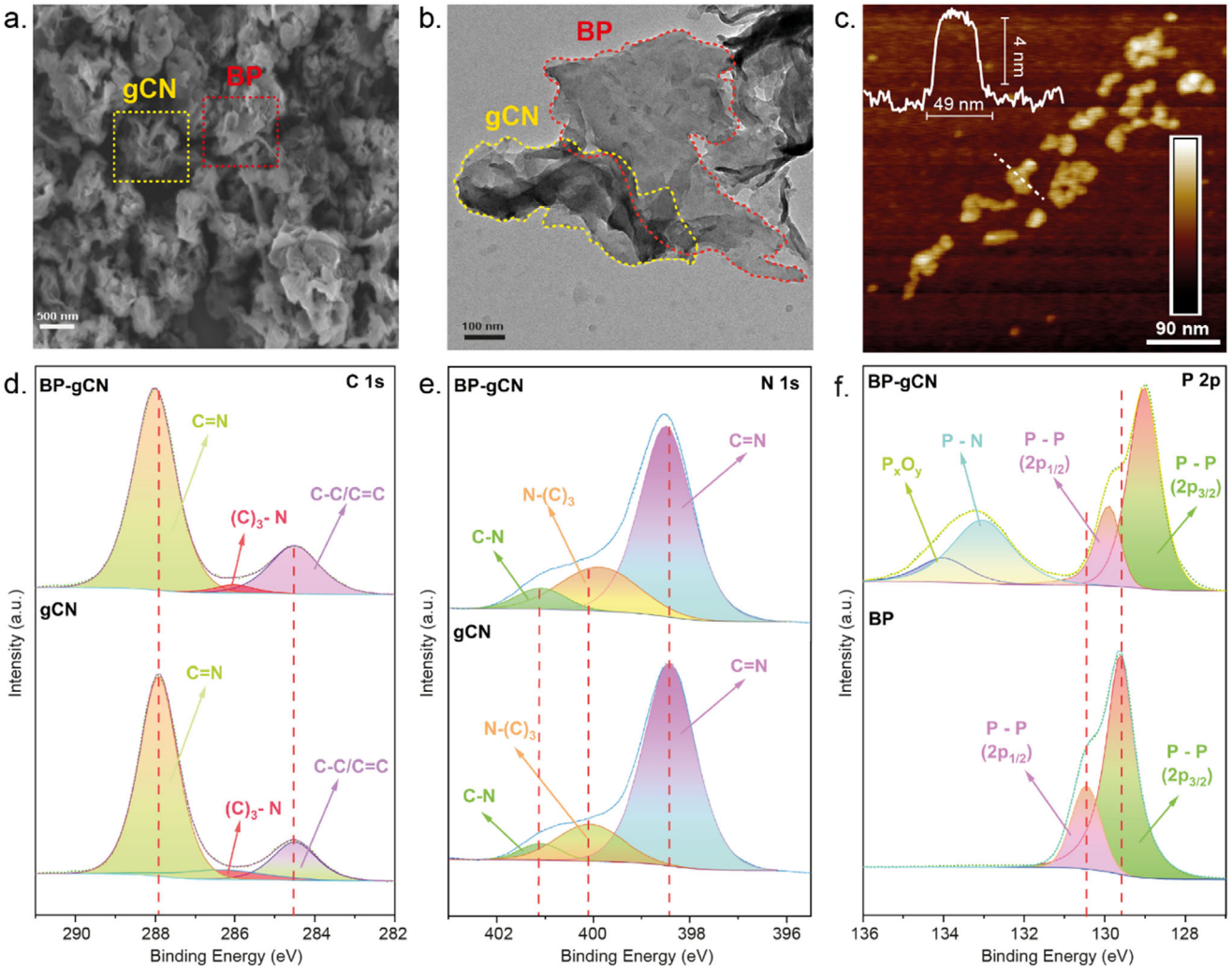


Figure 2. Characterization of pristine BP, pristine gCN, and BP-gCN heterostructure. a) SEM image b) TEM image and c) AFM image with the inset of the height profile of the BP-gCN heterostructures. XPS spectrum of d) C1s, e) N 1s, f) P 2p for pristine gCN, pristine BP (bottom) and BP-gCN heterostructure (top).

2.2. Performance and Characterization of the Electrochemical Sensor

Following material characterization, the intrinsic electrochemical properties of various BP-gCN compositions (5, 10, 15, and 20 wt% BP) were evaluated. Cyclic Voltammetry (CV) measurements were conducted in a standard redox probe solution of $K_3[Fe(CN)_6]$ (in 0.1 M KCl) over a potential range of +1 V to −1 V at a scan rate of 0.02 V s^{-1}, providing a baseline for assessing electron transfer efficiency. As illustrated in the CV graphs (**Figure** 3a) and the corresponding peak current bar graph (Figure 3b), the 10 wt% BP-gCN heterostructure demonstrated the highest current density and best peak resolution among the tested compositions. This indicates that the 10 wt% BP-gCN composition exhibits the most favorable combination of active site availability and electron transfer efficiency. At lower BP content (5 wt%), the BP domains may be insufficient to contribute significantly to redox-active sites.[58] On the other hand, at higher BP loading (20 wt%), aggregation or stacking of BP sheets could reduce the effective surface area and electron accessibility, thereby lowering the overall electrochemical response. The improved charge transfer kinetics arise from the synergistic effect of newly formed redox-active sites on oBP, as confirmed by Raman and XPS analyses, combined with the large surface area of gCN, collectively enabling more efficient electron transport and abundant active sites for glucose oxidation.

To emphasize the critical role of incorporating BP into gCN, we compared the Electrochemical Impedance Spectroscopy (EIS) and ECSA. The Nyquist plots obtained from EIS measurements were used to compare the charge transfer resistance of gCN (red) and BP-gCN (black) (Figure 3c). The inset illustrates the equivalent circuit model used to fit the EIS Nyquist plot, which includes several key elements: the resistance of the electrolyte solution (R_s), the Warburg element associated with the diffusion of the redox probe, the constant phase element (CPE), and R_{ct}. The BP-gCN heterostructure exhibits a smaller semicircle in the Nyquist plot compared to pristine gCN, signifying a faster charge

© 2025 The Author(s). Advanced Materials Technologies published by Wiley-VCH GmbH

2365709x, 2025, 17, Downloaded from https://advanced.onlinelibrary.wiley.com/doi/10.1002/admt.202500106 by Koc University, Wiley Online Library on [05/12/2025]. See the Terms and Conditions (https://onlinelibrary.wiley.com/terms-and-conditions) on Wiley Online Library for rules of use; OA articles are governed by the applicable Creative Commons License

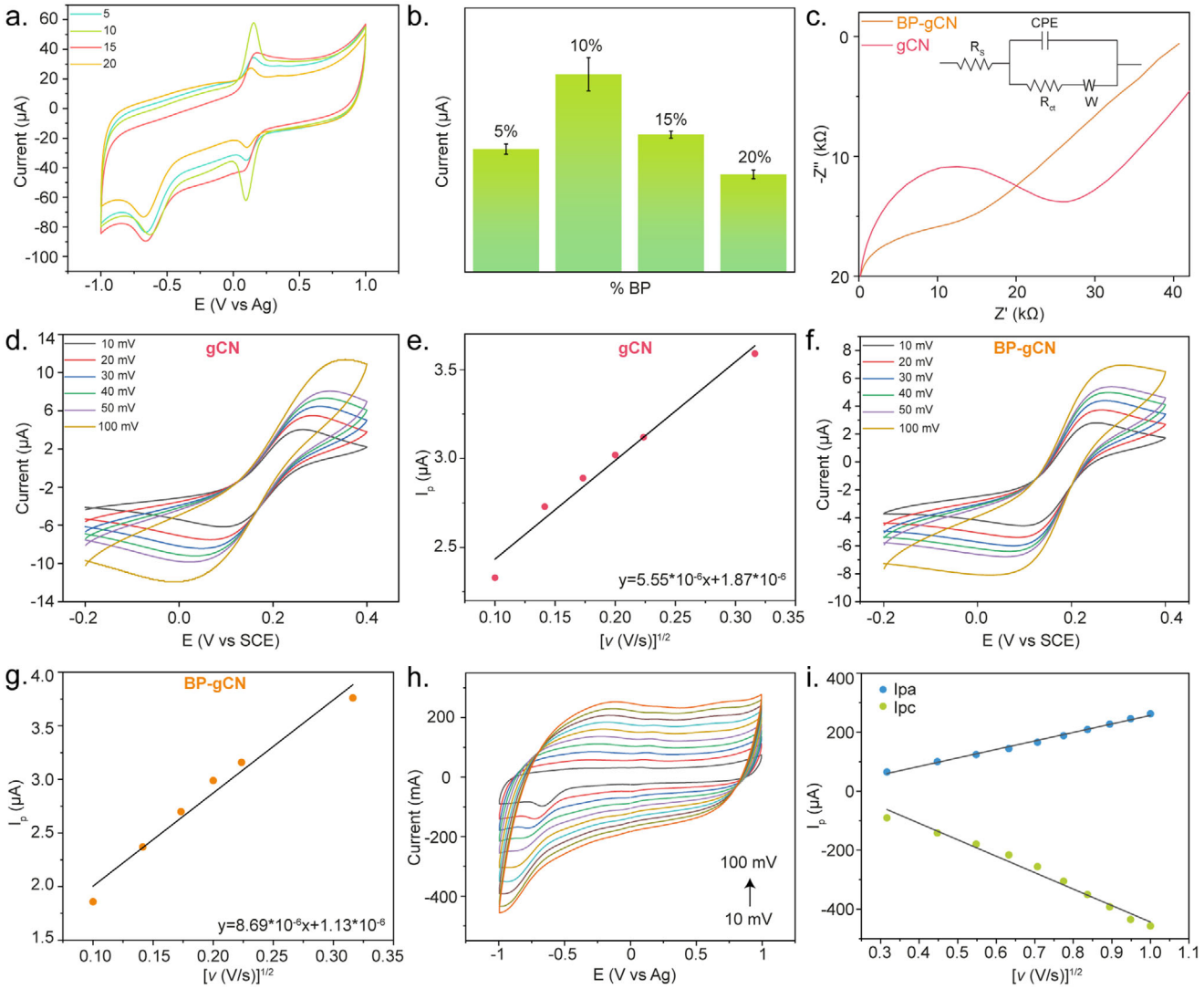


Figure 3. The electrochemical characterization of pristine gCN and BP-gCN heterostructure. a) CV comparison of (5–20% wt) BP-gCN and b) corresponding bar graph for electrocatalytic activity at Ip_a c) Nyquist plot of gCN and BP-gCN (inset equivalent circuit model used for fitting). CV graphs at various scan rates for d) gCN and e) BP-gCN in $K_3[Fe(CN)_6]$. f) CV graphs at various scan rates for BP-gCN in 1 mM glucose. Corresponding linear fittings for Randles-Sevcik equations; g) gCN, h) BP-gCN, i) BP-gCN-1 mM glucose.

transfer at the interface and a 2 fold lower R_{ct}. As many studies have shown, a lower R_{ct} is generally indicative of improved sensor performance due to faster electron transfer kinetics at the electrode-electrolyte interface.[59] This enhanced electron transfer plays a critical role in promoting faster electron flow during the electrooxidation of glucose. This improvement can be attributed to the synergistic effects of BP and gCN, which facilitate better electron transport and conductivity in the heterostructure. The improved charge transfer properties of the BP-gCN heterostructure enhance the utilization of the combined active sites of both BP and gCN, ensuring that a larger number of active sites are effectively wired into the electrochemical process, making them readily accessible for the glucose oxidation reaction. Therefore, the Nyquist plots clearly demonstrate that the BP-gCN heterostructure exhibits a significantly lower R_{ct}, indicating a more facile electron transport pathway at the electrode-electrolyte interface, which is crucial for achieving enhanced sensor sensitivity. Overall, the lower impedance of BP-gCN suggests enhanced electrochemical performance, as lower impedance correlates with higher sensor sensitivity. Additionally, the ECSA was calculated using the Randles-Sevcik equation based on CV measurements at different scan rates for gCN (Figure 3d,e) and BP-gCN (Figure 3f,g). By substituting the relevant parameters into the equation, the results demonstrated that BP-gCN ECSA is 1.6 times greater than that of pristine gCN, offering a greater number of active sites for glucose adsorption and subsequent oxidation. The comparative analysis of EIS and ECSA highlights the significant enhancements achieved by the formation of the heterostructure between BP and gCN. The formation of the heterostructure not only increased active sites but also improved electron transfer kinetics, collectively contributing to the superior electrochemical performance observed in this study.

© 2025 The Author(s). Advanced Materials Technologies published by Wiley-VCH GmbH

2365709x, 2025, 17, Downloaded from https://advanced.onlinelibrary.wiley.com/doi/10.1002/admt.202500106 by Koc University, Wiley Online Library on [05/12/2025]. See the Terms and Conditions (https://onlinelibrary.wiley.com/terms-and-conditions) on Wiley Online Library for rules of use; OA articles are governed by the applicable Creative Commons License

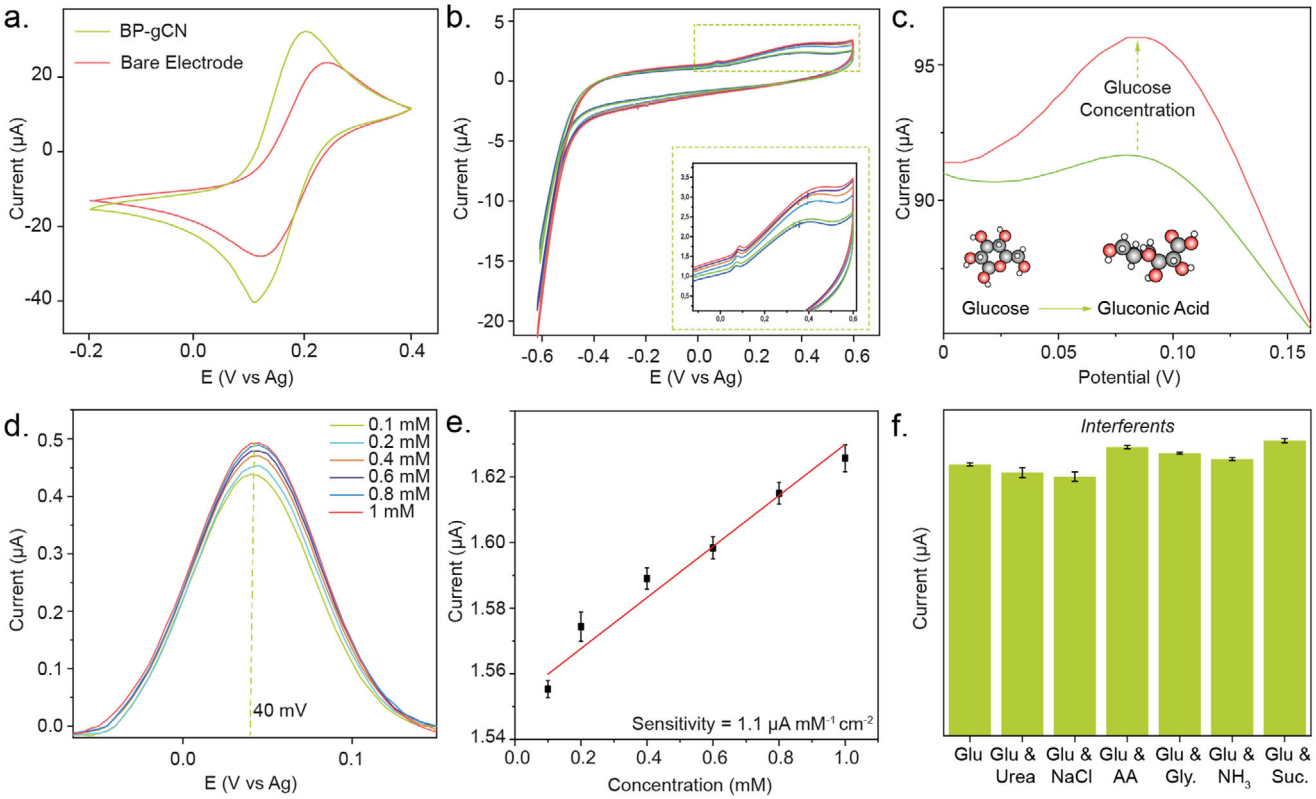


Figure 4. The electrochemical glucose sensing performance of BP-gCN. a) CV of 10% BP-gCN modified and bare SPCE in $K_3[Fe(CN)_6]$ between −0.2 V and +0 .4 V. b) Response of the sensor to glucose by CV in 0.1 X PBS solution (inset: anodic scan zoomed) c) Representation of glucose sensing mechanism of the proposed sensor. d) Response of the sensor to glucose by DPV. e) Corresponding calibration curve at 40 mV. f) Selectivity of the sensor with main interferents (Urea, NaCl, ascorbic acid, glycine, sucrose, NH_3) showing a slight change in the sensor's response compared to glucose.

To further gain a mechanistic understanding of how the glucose molecules interact with the BP-gCN electrocatalyst surface, CV measurements were conducted at various scan rates in 1 mM glucose (in PBS) solution (Figure 3h,i). The increase in both maximum and minimum peak currents with increasing scan rates suggests that the electrochemical process is diffusion-controlled, as supported by the linearity of the curve obtained from the square root of scan rate data in accordance with the Randles-Sevcik equation. Complementing these findings, the lower frequency region of EIS plot shows the presence of the Warburg element, which signifies the effect of diffusion limitation on overall electrochemical reaction kinetics. The Warburg element of BP-gCN has a reduced slope compared to that of gCN, indicating reduced diffusion limitations, improved mass transport, and consequently a faster electrochemical response.

After determining the optimal composition, further electrochemical characterizations were conducted with the 10 wt% BP-gCN modified electrode in PBS (pH = 7.0) to evaluate the sensitivity, selectivity, stability, and concentration dependence of the sensor toward glucose oxidation under physiological conditions ex situ. First, the electrocatalytic activities of modified and un-modified electrodes were compared in 5 mM $K_3[Fe(CN)_6]$ (0.1 M KCl), showing increased activity for the modified electrode (**Figure** 4a). For the glucose sensing experiment, CV was employed to identify the oxidation potential of glucose (1–10 mM in PBS) in the anodic scan. According to Figure 4b, oxidation of glucose starts after 0 V, and peak separation at the lowest potential is observed at 40 mV. Following this, Figure 4c illustrates the representative sensing mechanism, detailing the oxidation of glucose to gluconic acid. The oxidation products were confirmed through quadrupole time-of-flight mass spectrometry (qTOF-MS), elucidating the electrochemical pathways involved. According to qTOF-MS spectra (Figure S7, Supporting Information), the main product of glucose oxidation is observed as gluconic acid at 219.04 m z^{-1}, indicated by the highest peak intensity.

Differential pulse voltammetry (DPV), a sensitive technique ideal for detecting low-concentration analytes, was performed between −0.2 V and +0.4 V on glucose solutions ranging from 0 to 1 mM in 0.2 mM increments -levels relevant to physiological sweat glucose- enabling precise quantification of glucose oxidation currents as shown in Figure 4d.[60] Additionally, a calibration curve obtained from DPV graphs (Figure 4e) at 40 mV was plotted with n = 3. The slope of the calibration curve was used as the sensitivity output as suggested by IUPAC,[61] and the calculated sensitivity of the proposed sensor was obtained as 1.1 μA mM^{-1} cm^{-2}.

To gain a deeper understanding of the sensor's performance characteristics, we assessed the stability and selectivity of the fabricated sensors. Sensor performance was evaluated in artificial sweat with various pH values (pH 6, pH 7, and pH 8) by adjusting the pH of the solution. Increasing concentrations of glucose were evaluated by CV for each pH value, and

© 2025 The Author(s). Advanced Materials Technologies published by Wiley-VCH GmbH

2365709x, 2025, 17, Downloaded from https://advanced.onlinelibrary.wiley.com/doi/10.1002/admt.202500106 by Koc University, Wiley Online Library on [05/12/2025]. See the Terms and Conditions (https://onlinelibrary.wiley.com/terms-and-conditions) on Wiley Online Library for rules of use; OA articles are governed by the applicable Creative Commons License

corresponding calibration curves were obtained for comparison. As shown in Figure S8a–d (Supporting Information), the sensor exhibits good sensitivity across the physiologically relevant pH range of sweat. Notably, the sensor demonstrated the highest sensitivity at pH 6. This observation is particularly promising for the device's effectiveness in real-world conditions, as the pH of sweat (≈6.3) is typically more acidic than that of blood.[62] Furthermore, the sensitivity values obtained from CV measurements were significantly higher than those obtained from DPV experiments. This difference is attributed to the fundamental differences between the techniques: CV measurements include both Faradaic currents (from oxidation-reduction reactions) and non-Faradaic currents (capacitive effects), while DPV is designed to minimize capacitive currents, providing a more selective measurement of Faradaic currents from glucose oxidation.[63] To assess the reproducibility of the measurements in a complex medium, artificial sweat glucose experiments were also conducted using DPV with three repetitions (n = 3), yielding a sensitivity of 4.75 μA mM^{-1} cm^{-2} at 0.075 V peak current (Figure S8f,e, Supporting Information). These results align with our previous findings, where the sensitivity in PBS was 1.1 μA mM^{-1} cm^{-2} (calculated for peak current values at 0.04 V) and further confirm the higher sensitivity observed in artificial sweat compared to PBS. This difference in sensitivity at peak current potential is due to variations in ionic conductivity and glucose diffusion dynamics between the two solutions. The stability of the 10% BP-gCN-based sensor was evaluated through CV over 50 cycles, demonstrating a peak current retention of 84% as illustrated in Figure S9 (Supporting Information). The long-term stability of the BP-gCN is attributed to the surface oxide layer on BP, which forms P—O bonds through partial oxidation while protecting the underlying BP.[64,65] Furthermore, the formation of P—O bonds enhances the surface hydrophilicity, making it suitable for sensor applications.

Given the complex nature of human sweat, which contains various common electroactive interferents, it is of great importance that a sensor used in a wearable device can selectively and accurately sense glucose. Therefore, we also examined the selectivity of the sweat analyte sensor. To comprehensively assess the sensor's selectivity, we performed a selectivity test (n = 3) where the sensor's response to 1 mM glucose was measured in the presence of various interfering species, including ascorbic acid, urea, NaCl, sucrose, glycine, and NH_3. As shown in Figure 4f, the presence of these potential interferents resulted in only relatively small changes in the sensor's response to glucose. The change in signal for all interferents was within ± 10% of the response to glucose alone, demonstrating that these compounds do not significantly interfere with glucose detection under our experimental conditions. The observed high selectivity of the BP-gCN heterostructure-based sensor can be attributed to several factors. Typically, nonenzymatic sensors require high working potential, which can lead to the oxidation of other electroactive interferents, such as ascorbic acid. However, we addressed this issue by employing a low working potential for the sensor. Additionally, the selective behavior of the BP-gCN can be attributed to the heterostructure's negative surface charge, which promotes selective adsorption of glucose while repelling negatively charged species present in the sweat.[66,67]

2.3. Computational Study

To investigate and compare the glucose sensing performances of gCN and BP-gCN, DFT calculations were conducted. First, the planar structures of the pristine gCN and BP surfaces were optimized and a model of the BP-gCN heterostructure was constructed as illustrated in Figure S10 (Supporting Information). It can be seen that both pristine gCN and BP monolayers become wrinkled when a heterojunction is formed between them. This wrinkling occurs as a result of the strong interactions due to P-N bond formation, which are not present in their pristine forms. This structural transformation can enhance the surface properties of the heterojunction, potentially promoting stronger glucose adsorption, which accounts for the electrocatalytic activity of glucose oxidation.[68,69] Therefore, we examined the glucose adsorption on the planar gCN surface and found that this interaction also induced a structural transformation of the gCN layer from planar to wrinkled (Figure S11a, Supporting Information). As illustrated in Figure S11b (Supporting Information), this wrinkled structure persisted even after the glucose molecule was removed. Interestingly, a previous study also reported an irreversible transformation of the gCN monolayer from a planar to a wrinkled structure after the C_{60} adsorption.[70] It was also determined that the wrinkled gCN structure is more stable than the planar structure, with its energy being 4.55 eV lower. Therefore, we proceeded with our DFT calculations using wrinkled gCN and subsequently calculated the glucose adsorption energy (ΔE) on this structure, obtaining a value of −1.04 eV.

As previously discussed in the experimental section, XPS and Raman analysis of the BP-gCN heterostructures revealed the formation of native surface oxides. Based on these findings, we investigated the role of O species on the BP surface. To represent the oxidized BP-gCN catalyst, we constructed the surface-oxidized BP-gCN-O_{14} structure, following the approach of previous studies.[57,71] Our DFT calculations provided further evidence of the distinct role of BP sites in oxygen interaction. The adsorption energy calculations revealed that oxygen binds much more strongly to BP within the heterostructure (−2.73 eV) than to gCN sites (−0.43 eV), confirming BP as the preferred site for oxide formation in the composite structure. Glucose adsorption was compared between BP-gCN-O_1, a heterostructure with a single oxygen atom, and BP-gCN-O_{14}, which features multiple surface oxygen atoms. As shown in Figure S12 (Supporting Information), BP-gCN-O_1 does not significantly stabilize the glucose molecule compared to BP-gCN-O_{14}, highlighting the role of increased surface oxygen coverage in enhancing glucose adsorption. Notably, our calculations show that glucose exhibits significantly stronger adsorption on BP-gCN-O_{14} compared to wrinkled gCN, with ΔE of −1.42 eV and −1.04 eV, respectively, as shown in **Figure 5**a,b. These results highlight enhanced glucose adsorption on the heterostructure, supporting our approach of utilizing the heterojunction over pristine structures.

To elucidate the stronger glucose binding affinity to BP-gCN-O_{14} compared to gCN, we calculated the projected density of states (PDOS) for these surfaces. The analysis focused on the short bonds between glucose and surface atoms (≤2.1 Å), which are indicative of strong interactions. Figure S13a,b (Supporting Information) illustrates that for gCN, one H—N bond is formed with a bond length of 1.87 Å, whereas for BP-gCN-O_{14}, four H—O

© 2025 The Author(s). Advanced Materials Technologies published by Wiley-VCH GmbH

2365709x, 2025, 17, Downloaded from https://advanced.onlinelibrary.wiley.com/doi/10.1002/admt.202500106 by Koc University, Wiley Online Library on [05/12/2025]. See the Terms and Conditions (https://onlinelibrary.wiley.com/terms-and-conditions) on Wiley Online Library for rules of use; OA articles are governed by the applicable Creative Commons License

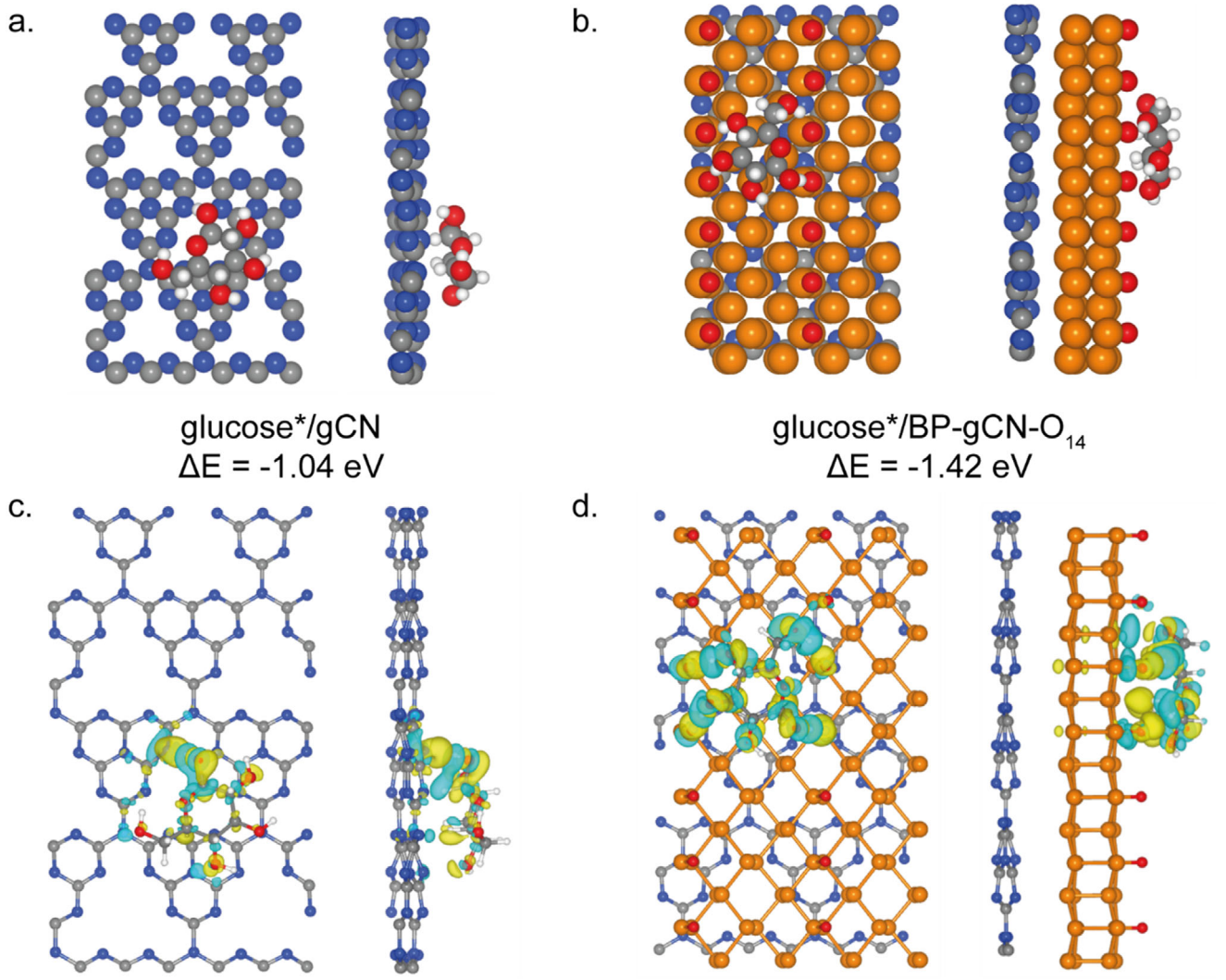


Figure 5. Theoretical analysis of glucose adsorption on electrocatalyst surfaces. Top and side views of glucose adsorption on a) wrinkled gCN and b) BP-gCN-O_{14} with corresponding adsorption energies (ΔE). Differential charge densities of c) gCN and d) BP-gCN-O_{14} after glucose adsorption. Yellow and cyan isosurfaces (±0.001 e/Bohr^3) represent charge accumulation and depletion, respectively. Atom color codes: blue (N), gray (C), orange (P), red (O), white (H).

bonds are formed with bond lengths ranging from 1.73 to 2.11 Å. Accordingly, in Figure S13c,d (Supporting Information), we analyzed the PDOS of the H atoms participating in the strong binding to gCN and BP-gCN-O_{14}, along with the relevant surface atoms. It can be observed that there is some degree of hybridization between the N states of gCN and the H states of glucose. However, there is a more pronounced hybridization between the O states of BP-gCN-O_{14} and the H states of glucose, resulting in stronger glucose adsorption. Additionally, we performed a Bader charge analysis to investigate the charge transfer between the adsorbed glucose molecule and the catalyst surfaces. The results show that the gCN surface slightly loses electrons (+0.02 |e|), while the BP-gCN-O_{14} surface gains electrons (−0.14 |e|) upon glucose adsorption, as illustrated in the electron density difference plots in Figure 5c,d. Since the sensor sensitivity typically depends on the charge transfer amount after adsorption,[72] these results reveal that BP-gCN-O_{14} exhibits better glucose sensing ability compared to the pristine gCN. Overall, our theoretical findings provide a comprehensive explanation for the superior glucose sensing performance of oBP-gCN observed experimentally.

2.4. Wearable Patch Fabrication and On-Body Evaluation

As summarized in Table S1 (Supporting Information), previous studies on nonenzymatic electrochemical glucose sensors often involved metal-containing catalysts. While these metal-based sensors can exhibit good sensitivity, potentially due to the catalytic activity of the metals and often operating in alkaline media which can enhance the electrochemical reaction, their translation into fully functional wearable devices for direct, real-time on-body applications has remained a significant challenge. In contrast, our work presents the first demonstration of a fully metal-free gCN-based sensor within a fully integrated wearable device for

© 2025 The Author(s). Advanced Materials Technologies published by Wiley-VCH GmbH

2365709x, 2025, 17, Downloaded from https://advanced.onlinelibrary.wiley.com/doi/10.1002/admt.202500106 by Koc University, Wiley Online Library on [05/12/2025]. See the Terms and Conditions (https://onlinelibrary.wiley.com/terms-and-conditions) on Wiley Online Library for rules of use; OA articles are governed by the applicable Creative Commons License

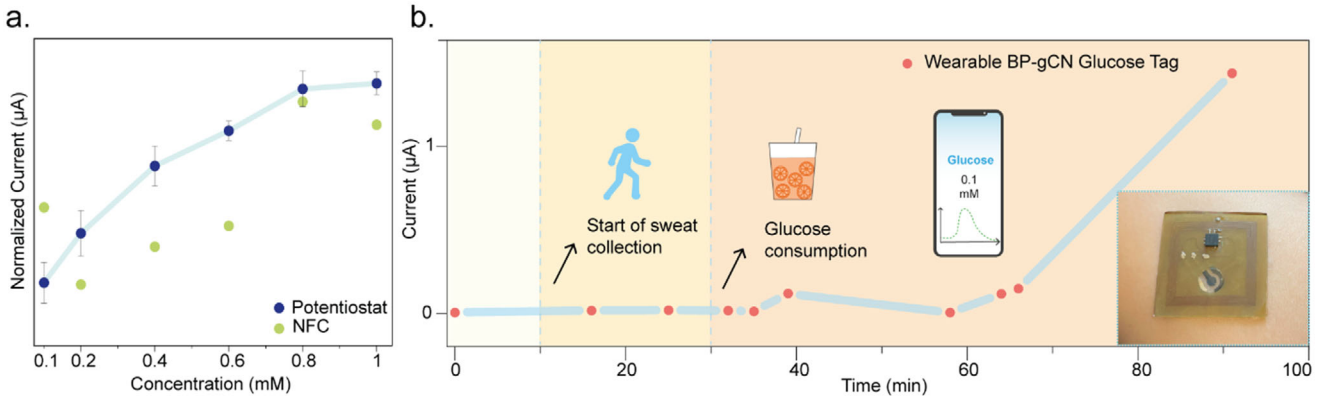


Figure 6. Integration of BP-gCN to wearable NFC based glucose monitoring patch. a) Correlation between bench-top potentiostat and NFC development kit for glucose in artificial sweat. b) Results of the on-body experiment, showing a dramatic increase after orange juice intake at the 90th min (Inset image: Non-enzymatic wearable glucose patch worn on the subject's arm).

continuous, nonenzymatic glucose monitoring directly on the body. Despite being metal-free, our BP-gCN sensor achieves a comparable sensitivity (1.1 μA mM^{-1} cm^{-2} in PBS and 4.75 μA mM^{-1} cm^{-2} in artificial sweat) to some of these metal-based sensors, while uniquely enabling direct on-body measurement in a wearable format. This combination of a metal-free composition and a demonstrated pathway for practical wearable application represents a significant advancement over many existing nonenzymatic sensor studies that rely on metal catalysts and lack critical real-world validation. Beyond its metal-free nature and wearable integration, our BP-gCN sensor's notably low working potential (0.04 V in PBS, 0.075 V in artificial sweat) also makes this device energy efficient for wearable applications. To further validate the potential of BP-gCN sensor for real-world glucose monitoring, we conducted a comprehensive evaluation involving initial benchtop experiments followed by in vivo testing on human subjects.

Initially, benchtop experiments were conducted in PBS and artificial sweat solution for various glucose concentrations. **Figure** 6a demonstrates the correlation between the calibration curves obtained from the potentiostat and the NFC development kit, confirming the ability of the BP-gCN sensor to be integrated into wearable devices for glucose detection in sweat. Building on our earlier report, where we detailed the fabrication process for wearable enzymatic glucose sensors,[73] a similar approach was applied in this work, allowing for a seamless transition to nonenzymatic sensing applications. Briefly, the wearable device is composed of several key components: an NFC chip that handles both sensor reading and data processing, an antenna that provides wireless power and facilitates data communication with a smartphone, and microfluidic channels, which transport sweat from the skin to the glucose sensor. The in vivo physical exercise test, depicted in Figure 6b, shows the successful application of the metal-free, nonenzymatic wearable sensor for real-time glucose monitoring in sweat during treadmill running. Initial readings were obtained while the subject was running prior to consuming any food or drink. Following these initial readings, the subject consumed orange juice at the 30 min mark and resumed running on the treadmill. New data were then collected to analyze the changes in the glucose profile in sweat resulting from the orange juice intake. The increase in sweat glucose level was observed 1 h after consumption, consistent with the typical delay in the response between blood and sweat glucose concentrations. These findings demonstrate the device's applicability in in vivo settings. The integration of NFC technology, enables continuous, real-time glucose monitoring, offering a promising solution for nonintrusive and wearable glucose analysis under physiological conditions.

3. Conclusion

This study presents a battery-free, flexible, nonenzymatic wearable glucose sensor based on BP-gCN heterostructures, offering a robust platform for real-time, non-invasive sweat glucose monitoring. The integration of rational material design and wearable technology enabled the development of a high-performance sensing device with a sensitivity of 4.75 μA mM^{-1} cm^{-2} under physiological conditions. The superior glucose oxidation activity of the BP-gCN heterostructures was attributed to the engineered P-N interactions, which significantly enhanced the electrochemically active surface area and reduced the charge transfer resistance. Complementary DFT calculations provided further insights into the electronic properties of the heterostructures, demonstrating stronger glucose adsorption and enhanced charge transfer on the BP-gCN surface compared to the pristine gCN. The device's applicability was also validated through on-body tests, where the conformal battery-free wearable patch enabled reliable, wireless glucose monitoring via an NFC-based smartphone application. The high sensitivity and stability under physiological conditions highlight the potential of BP-gCN heterostructures for addressing challenges in continuous glucose monitoring. This work not only demonstrates a scalable and biocompatible platform for sweat-based glucose sensing but also paves the way for the development of advanced nanomaterial-based wearable sensors. Future research can explore novel metal-free nanomaterials for higher sensitivity or extend their application to multi-analyte detection, unlocking new possibilities for next-generation wearable biosensing technologies tailored for personalized health monitoring.

© 2025 The Author(s). Advanced Materials Technologies published by Wiley-VCH GmbH

2365709x, 2025, 17, Downloaded from https://advanced.onlinelibrary.wiley.com/doi/10.1002/admt.202500106 by Koc University, Wiley Online Library on [05/12/2025]. See the Terms and Conditions (https://onlinelibrary.wiley.com/terms-and-conditions) on Wiley Online Library for rules of use; OA articles are governed by the applicable Creative Commons License

4. Experimental Section

The experimental details are provided in the Supporting Information.

Supporting Information

Supporting Information is available from the Wiley Online Library or from the author.

Acknowledgements

The authors thank Buse Sundu for TEM imaging, Barıs Yagcı for SEM imaging, Hande Gunduz for qTOF-MS measurements, and Alp Timucin Toymus for constructive feedback on the manuscript preparation. The individual whose data contributes to in vivo experiments willingly participated in the experiment and provided informed consent for their involvement in the study. The authors acknowledge the use of the services and facilities of Koç University Surface Science and Technology Center (KUYTAM) and n^{2}STAR-Koç University Nanofabrication and Nanocharacterization Center for Scientific and Technological Advanced Research. The computational part of this work was performed at the High Performance Grid Computing Center (Tr-Grid e-infrastructure), the Scientific and Technological Research Council of Türkiye (TUBITAK) ULAKBIM. E.E.O. is supported by TUBITAK through the 2211/A program. O.M. acknowledges the Turkish Academy of Sciences (TUBA) for the partial financial support. L.B. acknowledges (TUBITAK) as the project received funding from 2232 program (Grant No. 118C295) and 3501 program (Grant No. 120M363).

Conflict of Interest

The authors declare no conflict of interest.

Data Availability Statement

The data that support the findings of this study are available from the corresponding author upon reasonable request.

Keywords

black phosphorus, density functional theory, electrochemical sensors, graphitic carbon nitride, heterostructure, nonenzymatic glucose sensors, wearable devices

Received: January 15, 2025
Revised: May 9, 2025
Published online: May 24, 2025

[1] M. Bariya, H. Y. Y. Nyein, A. Javey, *Nat. Electron.* **2018**, *1*, 160.
[2] W. Gao, S. Emaminejad, H. Y. Y. Nyein, S. Challa, K. Chen, A. Peck, H. M. Fahad, H. Ota, H. Shiraki, D. Kiriya, D. H. Lien, G. A. Brooks, R. W. Davis, A. Javey, *Nature* **2016**, *529*, 509.
[3] A. J. Bandodkar, W. J. Jeang, R. Ghaffari, J. A. Rogers, *Annu. Rev. Anal. Chem.* **2019**, *12*, 1.
[4] M. Bariya, Z. Shahpar, H. Park, J. Sun, Y. Jung, W. Gao, H. Y. Y. Nyein, T. S. Liaw, L. C. Tai, Q. P. Ngo, M. Chao, Y. Zhao, M. Hettick, G. Cho, A. Javey, *ACS Nano* **2018**, *12*, 6978.
[5] P. P. Samant, M. M. Niedzwiecki, N. Raviele, V. Tran, J. Mena-Lapaix, D. I. Walker, E. I. Felner, D. P. Jones, G. W. Miller, M. R. Prausnitz, *Sci. Transl. Med.* **2020**, *12*, 1.
[6] Z. Yuan, H. Li, Z. Duan, Q. Huang, M. Zhang, H. Zhang, J. Guo, Y. Jiang, H. Tai, *Sensors Actuators A Phys.* **2024**, *369*, 115202.
[7] Q. Huang, Y. Jiang, Z. Duan, Y. Wu, Z. Yuan, M. Zhang, Q. Zhao, Y. Zhang, B. Liu, H. Tai, *Nano Energy* **2023**, *118*, 108997.
[8] J. R. Sempionatto, L. C. Brazaca, L. García-Carmona, G. Bolat, A. S. Campbell, A. Martin, G. Tang, R. Shah, R. K. Mishra, J. Kim, V. Zucolotto, A. Escarpa, J. Wang, *Biosens. Bioelectron.* **2019**, *137*, 161.
[9] R. C. Tseng, C. C. Chen, S. M. Hsu, H. S. Chuang, *Sensors (Switzerland)* **2018**, *18*, 2651.
[10] J. Zhao, H. Y. Y. Nyein, L. Hou, Y. Lin, M. Bariya, C. H. Ahn, W. Ji, Z. Fan, A. Javey, *Adv. Mater.* **2021**, *33*, 1.
[11] M. S. Mannoor, H. Tao, J. D. Clayton, A. Sengupta, D. L. Kaplan, R. R. Naik, N. Verma, F. G. Omenetto, M. C. McAlpine, *Nat. Commun.* **2012**, *3*, 763.
[12] H. Lee, T. K. Choi, Y. B. Lee, H. R. Cho, R. Ghaffari, L. Wang, H. J. Choi, T. D. Chung, N. Lu, T. Hyeon, S. H. Choi, D. H. Kim, *Nat. Nanotechnol.* **2016**, *11*, 566.
[13] P. Zimmet, K. G. Alberti, D. J. Magliano, P. H. Bennett, *Nat. Rev. Endocrinol.* **2016**, *12*, 616.
[14] J. Kim, I. Jeerapan, S. Imani, T. N. Cho, A. Bandodkar, S. Cinti, P. P. Mercier, J. Wang, *ACS Sens.* **2016**, *1*, 1011.
[15] H. Mirzajani, E. Istif, T. Abbasiasl, F. Mirlou, E. E. Özkahraman, M. Hasanreisoglu, L. Beker, *Adv. Mater. Technol.* **2022**, *7*, 2101629.
[16] O. Parlak, S. T. Keene, A. Marais, V. F. Curto, A. Salleo, *Sci. Adv.* **2018**, *4*, aar2904.
[17] F. Gao, C. Liu, L. Zhang, T. Liu, Z. Wang, Z. Song, H. Cai, Z. Fang, J. Chen, J. Wang, M. Han, J. Wang, K. Lin, R. Wang, M. Li, Q. Mei, X. Ma, S. Liang, G. Gou, N. Xue, *Microsystems Nanoeng.* **2023**, *9*, 1.
[18] X. He, T. Xu, Z. Gu, W. Gao, L. P. Xu, T. Pan, X. Zhang, *Anal. Chem.* **2019**, *91*, 4296.
[19] J. W. Liu, Y. Luo, Y. M. Wang, L. Y. Duan, J. H. Jiang, R. Q. Yu, *ACS Appl. Mater. Interfaces* **2016**, *8*, 33439.
[20] P. Liu, X. Huo, Y. Tang, J. Xu, X. Liu, D. K. Y. Wong, *Anal. Chim. Acta* **2017**, *984*, 86.
[21] J. R. Sempionatto, M. Lin, L. Yin, E. De la paz, K. Pei, T. Sonsa-ard, A. N. de Loyola Silva, A. A. Khorshed, F. Zhang, N. Tostado, S. Xu, J. Wang, *Nat. Biomed. Eng.* **2021**, *5*, 737.
[22] M. D. Steinberg, P. Kassal, I. M. Steinberg, Y. Yang, Y. Song, X. Bo, J. Min, O. S. Pak, L. Zhu, M. Wang, J. Tu, A. Kogan, H. Zhang, T. K. Hsiai, Z. Li, W. Gao, T. Terse-Thakoor, M. Punjiya, Z. Matharu, B. Lyu, M. Ahmad, G. E. Giles, R. Owyeung, F. Alaimo, M. Shojaei Baghini, T. T. Brunyé, S. Sonkusale, M. D. Steinberg, P. Kassal, I. M. Steinberg, *Electroanalysis* **2016**, *28*, 1149.
[23] J. Morshed, R. Nakagawa, M. M. Hossain, Y. Nishina, S. Tsujimura, *Biosens. Bioelectron.* **2021**, *189*, 113357.
[24] F. Tehrani, H. Teymourian, B. Wuerstle, J. Kavner, R. Patel, A. Furmidge, R. Aghavali, H. Hosseini-Toudeshki, C. Brown, F. Zhang, K. Mahato, Z. Li, A. Barfidokht, L. Yin, P. Warren, N. Huang, Z. Patel, P. P. Mercier, J. Wang, *Nat. Biomed. Eng.* **2022**, *6*, 1214.
[25] S. Park, H. Boo, T. D. Chung, *Anal. Chim. Acta* **2006**, *556*, 46.
[26] F. Xie, Z. Huang, C. Chen, Q. Xie, Y. Huang, C. Qin, Y. Liu, Z. Su, S. Yao, *Electrochem. Commun.* **2012**, *18*, 108.
[27] X. Zeng, Y. Zhang, X. Du, Y. Li, W. Tang, *New J. Chem.* **2018**, *42*, 11944.
[28] S. Sedaghat, C. R. Piepenburg, A. Zareei, Z. Qi, S. Peana, H. Wang, R. Rahimi, *ACS Appl. Nano Mater.* **2020**, *3*, 5260.
[29] C. Zhou, L. Xu, J. Song, R. Xing, S. Xu, D. Liu, H. Song, *Sci. Rep.* **2014**, *4*, 1.
[30] S. Bag, A. Baksi, S. H. Nandam, D. Wang, D. Wang, X. Ye, J. Ghosh, T. Pradeep, H. Hahn, H. Hahn, *ACS Nano* **2020**, *14*, 5543.
[31] J. Wang, D. F. Thomas, A. Chen, *Analyt. Chem.* **2008**, *80*, 997.
[32] R. Li, X. Deng, L. Xia, *Sci. Rep.* **2020**, *10*, 1.
[33] Z. Golsanamlou, M. Mahmoudpour, J. Soleymani, A. Jouyban, *Crit. Rev. Anal. Chem.* **2021**, *53*, 1116.
[34] X. Zhu, Y. Ju, J. Chen, D. Liu, H. Liu, *ACS Sens.* **2018**, *3*, 1135.

© 2025 The Author(s). Advanced Materials Technologies published by Wiley-VCH GmbH

2365709x, 2025, 17, Downloaded from https://advanced.onlinelibrary.wiley.com/doi/10.1002/admt.202500106 by Koc University, Wiley Online Library on [05/12/2025]. See the Terms and Conditions (https://onlinelibrary.wiley.com/terms-and-conditions) on Wiley Online Library for rules of use; OA articles are governed by the applicable Creative Commons License

[35] X. Strakosas, J. Selberg, P. Pansodtee, N. Yonas, P. Manapongpun, M. Teodorescu, M. Rolandi, *Sci. Rep.* **2019**, *9*, 1.
[36] D. Thirumalai, D. Subramani, B. Shin, H. J. Paik, S. C. Chang, *Bull. Korean Chem. Soc.* **2018**, *39*, 141.
[37] S. Wustoni, A. Savva, R. Sun, E. Bihar, S. Inal, *Adv. Mater. Interfaces* **2019**, *6*, 1.
[38] H. Imran, P. N. Manikandan, V. Dharuman, *Microchem. J.* **2021**, *160*, 105774.
[39] S. Vinoth, K. S. Shalini Devi, A. Pandikumar, *TrAC - Trends Anal. Chem.* **2021**, *140*, 116274.
[40] Z. Eroglu, M. S. Ozer, Ö. Metin, *ChemCatChem* **2024**, *16*, 202301560.
[41] J. Tian, Q. Liu, C. Ge, Z. Xing, A. M. Asiri, A. O. Al-Youbi, X. Sun, *Nanoscale* **2013**, *5*, 8921.
[42] S. Vinoth, P. M. Rajaitha, A. Venkadesh, K. S. Shalini Devi, S. Radhakrishnan, A. Pandikumar, *Nanoscale Adv.* **2020**, *2*, 4242.
[43] J. Tashkhourian, S. F. Nami-Ana, M. Shamsipur, *Anal. Chim. Acta* **2018**, *1034*, 63.
[44] L. Liu, M. Wang, C. Wang, *Electrochim. Acta* **2018**, *265*, 275.
[45] M. A. Tapia, R. Gusmão, N. Serrano, Z. Sofer, C. Ariño, J. M. Díaz-Cruz, M. Esteban, *TrAC - Trends Anal. Chem.* **2021**, *139*, 116249.
[46] C. Gu, X. Kong, S. Yan, P. Gai, F. Li, *ACS Sustainable Chem. Eng.* **2020**, *8*, 16549.
[47] H. Wang, H. Wang, J. Yang, P. Y. D. Maulida, J. Zou, Arramel, C. Wu, J. Jiang, *Carbon Lett.* **2023**, *33*, 2161.
[48] P. Nakhanivej, X. Yu, S. K. Park, S. Kim, J. Y. Hong, H. J. Kim, W. Lee, J. Y. Hwang, J. E. Yang, C. Wolverton, J. Kong, M. Chhowalla, H. S. Park, *Nat. Mater.* **2019**, *18*, 156.
[49] B. Han, Z. Duan, J. Xu, Y. Zhu, Q. Xu, H. Wang, H. Tai, J. Weng, Y. Zhao, *Adv. Funct. Mater.* **2020**, *30*, 2002232.
[50] Z. Eroglu, M. S. Ozer, T. Kubanaliev, H. Kilic, Ö. Metin, *Catal. Sci. Technol.* **2022**, *12*, 5379.
[51] M. Zhu, S. Kim, L. Mao, M. Fujitsuka, J. Zhang, X. Wang, T. Majima, *J. Am. Chem. Soc.* **2017**, *139*, 13234.
[52] Z. Eroglu, O. Metin, *ACS Appl. Nano Mater.* **2023**, *6*, 7960.
[53] E. Kalay, H. Küçükkeçeci, H. Kilic, Ö. Metin, *Chem. Commun.* **2020**, *56*, 5901.
[54] S. Wu, F. He, G. Xie, Z. Bian, J. Luo, S. Wen, *Nano Lett.* **2018**, *18*, 5618.
[55] J. W. Zhang, S. Gong, N. Mahmood, L. Pan, X. Zhang, J. J. Zou, *Appl. Catal. B Environ.* **2018**, *221*, 9.
[56] R. Cao, M. Q. Zhang, C. Hu, D. Xiao, M. Wang, D. Ma, *Nat. Commun.* **2022**, *13*, 4809.
[57] X. Wang, R. K. M. Raghupathy, C. J. Querebillo, Z. Liao, D. Li, K. Lin, M. Hantusch, Z. Sofer, B. Li, E. Zschech, I. M. Weidinger, T. D. Kühne, H. Mirhosseini, M. Yu, X. Feng, *Adv. Mater.* **2021**, *33*, 2008752.
[58] G. Yanalak, Z. Eroglu, S. Yılmaz, S. Z. Bas, O. Metin, I. H. Patir, *Int. J. Hydrogen Energy* **2023**, *48*, 14238.
[59] Y. Lei, D. Butler, M. C. Lucking, F. Zhang, T. Xia, K. Fujisawa, T. Granzier-Nakajima, R. Cruz-Silva, M. Endo, H. Terrones, M. Terrones, A. Ebrahimi, *Sci. Adv.* **2025**, *6*, abc4250.
[60] B. Zhang, Y. Zhang, J. Shen, Z. Zhou, G. Zhu, *Int. J. Electrochem. Sci.* **2024**, *19*, 100479.
[61] L. A. Currie, *Pure appl. chem.* **1995**, *67*, 16991723.
[62] Y. Yang, W. Gao, *Chem. Soc. Rev.* **2019**, *48*, 1465.
[63] N. Elgrishi, K. J. Rountree, B. D. McCarthy, E. S. Rountree, T. T. Eisenhart, J. L. Dempsey, *J. Chem. Educ.* **2018**, *95*, 197.
[64] M. T. Edmonds, A. Tadich, A. Carvalho, A. Ziletti, K. M. O'Donnell, S. P. Koenig, D. F. Coker, B. Özyilmaz, A. H. C. Neto, M. S. Fuhrer, *ACS Appl. Mater. Interfaces* **2015**, *7*, 14557.
[65] M. H. Jeong, D. H. Kwak, H. S. Ra, A. Y. Lee, J. S. Lee, *ACS Appl. Mater. Interfaces* **2018**, *10*, 19069.
[66] J. Liu, H. Wang, M. Antonietti, *Chem. Soc. Rev.* **2016**, *45*, 2308.
[67] J. Yi, X. Chen, Q. Weng, Y. Zhou, Z. Han, J. Chen, C. Li, *Electrochem. Commun.* **2020**, *118*, 106796.
[68] A. Caglar, D. Düzenli, I. Onal, I. Tezsevin, O. Sahin, H. Kivrak, *Int. J. Hydrogen Energy* **2020**, *45*, 490.
[69] R. Ponnusamy, R. Venkatesan, M. Kandasamy, B. Chakraborty, C. S. Rout, *Appl. Surf. Sci.* **2019**, *487*, 1033.
[70] X. Ma, X. Li, M. Li, X. Ma, L. Yu, Y. Dai, *Appl. Surf. Sci.* **2017**, *414*, 124.
[71] W. Zhai, Y. Chen, Y. Liu, Y. Ma, P. Vijayakumar, Y. Qin, Y. Qu, Z. Dai, *Nano-Micro Lett.* **2024**, *16*, 115.
[72] K. Devi P, K. K Singh, *Biosens. Bioelectron. X.* **2023**, *13*, 100287.
[73] H. Mirzajani, T. Abbasiasl, F. Mirlou, E. Istif, M. J. Bathaei, Ç. Dağ, O. Deyneli, D. Yazıcı, L. Beker, *Biosens. Bioelectron.* **2022**, *213*, 114450.

© 2025 The Author(s). Advanced Materials Technologies published by Wiley-VCH GmbH

2365709x, 2025, 17, Downloaded from https://advanced.onlinelibrary.wiley.com/doi/10.1002/admt.202500106 by Koc University, Wiley Online Library on [05/12/2025]. See the Terms and Conditions (https://onlinelibrary.wiley.com/terms-and-conditions) on Wiley Online Library for rules of use; OA articles are governed by the applicable Creative Commons License